




State transitions of a confined actomyosin system controlled through contractility and polymerization rate

Ryota Sakamoto ^{1,2,3,*} Makito Miyazaki ^{4,5,6,7} and Yusuke T. Maeda ^{1,*}

¹Department of Physics, Graduate School of Science, Kyushu University, 744 Motoooka, Nishi-ku, Fukuoka 819-0395, Japan

²Department of Biomedical Engineering, Yale University, 10 Hillhouse Avenue, New Haven, Connecticut 06520, USA

³Systems Biology Institute, Yale University, 850 West Campus Drive, West Haven, Connecticut 06516, USA

⁴Hakubi Center for Advanced Research, Kyoto University, Yoshida-honmachi, Sakyo-ku, Kyoto 606-8501, Japan

⁵Department of Physics, Graduate School of Science, Kyoto University, Kitashirakawa Oiwake-cho, Sakyo-ku, Kyoto 606-8502, Japan

⁶Institut Curie, PSL Research University, CNRS, UMR 144, F-75005 Paris, France

⁷PRESTO, JST, 4-1-8 Honcho, Kawaguchi, Saitama 332-0012, Japan



(Received 18 September 2022; accepted 14 February 2023; published 27 March 2023)

Pattern formation induced by symmetry breaking is a fundamental concept underlying biological phenomena across different scales, from single cells to tissues. However, the mechanics behind the pattern formation of the actomyosin system remains elusive due to complex biochemical regulations in living cells. In this study, we report the transition between distinct patterns of cytoplasmic actomyosin networks: steady actin flow and periodic actin waves, which are confined to a quasi-two-dimensional cell-like compartment. By combining molecular perturbations and numerical simulations of the active fluid model, we show that contractility and actin polymerization rate are the critical factors for the state transition from the steady actin flow to periodic actin waves. These patterns emerge either when active stress outweighs the diffusive relaxation of actin filaments or when the actin polymerization rate is sufficiently slow to accumulate actin filaments close to the surface of the circular confinement. Furthermore, our active fluid model predicts that the spatial heterogeneity at the onset of contraction leads to a rotational actin wave, which is stable only at the phase boundary between the steady actin flow and periodic actin waves. This study provides an integrative understanding of the distinct pattern formation of active gels confined in cell-sized spaces.

DOI: [10.1103/PhysRevResearch.5.013208](https://doi.org/10.1103/PhysRevResearch.5.013208)

Symmetry breaking is the basis of pattern formation in biological systems, from fish skin patterns [1] to the oscillatory pattern of the Min system in bacteria [2,3]. Such spatial pattern formation via translational symmetry breaking is often observed in reaction-diffusion systems. In reaction-diffusion systems of two species composed of an activator and an inhibitor, symmetry breaking arises from Turing instability, where the faster diffusion of the inhibitor stabilizes the small initial fluctuation in the spatial pattern [4]. Growing evidence suggests that the active cytoskeletal system, consisting of actin filaments and myosin molecular motors, plays an important role in achieving diverse pattern formation by harnessing its contractile forces [5–8]. Such actomyosin-involved symmetry breaking has been observed in various biological phenomena, including the chiral symmetry breaking of radial actin flow in fibroblasts [9], rotational waves in epithelial cells [10], rotational surface waves in dividing cells [11,12], and circular movement of blebs in *Xenopus* blastomeres [13].

Recent experiments have shown that Rho signaling is key to forming a reaction-diffusion pattern coupled with F-actin polymerization in the cell cortex [14,15]. However, the extent to which the mechanics of the actin cytoskeleton plays a role in driving pattern formation remains unclear. In theoretical studies, continuum mechanical models of the actin cytoskeleton on a flat cortex plane considering myosin contractility have shown that translational symmetry breaking can be achieved by the competition between active stress and diffusive relaxation [16–18]. Although these theoretical models showed that active force generation is a critical factor that causes the transition from the uniform state to ordered patterns in the actin cortex, such ordered patterns in experiments exhibit more diverse behaviors than theoretical predictions. Recent *in vivo* and *in vitro* experiments have shown that the combination of intracellular and cortical actomyosin networks induces distinct behaviors such as actin flow [19,20], periodic waves [21,22], rotational flows [9], and rotational waves [12], whereas how these distinct patterns emerge in the actomyosin system confined in small cell-sized spaces remains elusive.

In overcoming the difficulties in precisely controlling the biophysical parameters in living cells to compare the theoretical predictions with the experimental results, *in vitro* cell models composed of cytoplasmic actomyosin networks of *Xenopus laevis* egg extracts have been developed [20,21]. This reconstituted system allows us to flexibly control the biophysical parameters and develop simple theoretical models

* Author to whom all correspondence should be addressed: ryota.sakamoto@yale.edu; ymaeda@phys.kyushu-u.ac.jp

Published by the American Physical Society under the terms of the [Creative Commons Attribution 4.0 International](https://creativecommons.org/licenses/by/4.0/) license. Further distribution of this work must maintain attribution to the author(s) and the published article's title, journal citation, and DOI.

by decoupling mechanics from complex biochemical signaling [7,22–25]. *In vitro* systems using cytoplasmic actomyosin networks have revealed various self-organizations by harnessing the physiologically relevant actin turnover dynamics of the extracts, ranging from continuous actin flow [20,24] and periodic actomyosin contractions [21,22] to dynamic deformation and migration of droplets [26]. However, the physical mechanisms and molecular determinants of the emergence of these distinct self-organized states in the same actomyosin system remain poorly understood.

In this study, we realized both steady actin flow and ring-shaped periodic actin waves by encapsulating cytoplasmic actomyosin networks in a quasi-two-dimensional (quasi-2D) circular confinement composed of water-in-oil droplets. We demonstrated that the state transition can be controlled through contractility and polymerization rate by combining molecular perturbations and theoretical modeling of an active fluid model. Furthermore, our numerical simulation predicted the emergence of a rotational wave by imposing a time delay at the onset of contraction. This study revealed a physical mechanism of symmetry breaking and pattern formation of actomyosin networks confined in cell-sized spaces. The results provide an integrative physical understanding of biological pattern formation driven by active cytoskeletal systems.

I. RESULTS

A. Transition from steady actin flow to periodic actin waves

In the present study, we encapsulated the cytoplasmic actomyosin networks of M-phase *Xenopus* eggs into water-in-oil droplets covered with a phospholipid monolayer to develop a cell-like quasi-2D circular confinement ranging from a diameter of 200 to 300 μm [Figs. 1(a) and 1(b)]. *Xenopus* egg extracts contain physiological concentrations of various proteins required to perform F-actin polymerization/depolymerization and contraction of actomyosin networks, and the literature has revealed that the Arp2/3 complex is highly active in M-phase extracts [21]. Other studies encapsulating extracts into water-in-oil droplets have suggested that the recruitment of actin nucleation-promoting factor WASP at the water-oil interface may account for localized Arp2/3-mediated F-actin nucleation [20], and actomyosin contraction slows upon inhibition of Arp2/3 by CK666 [22].

In this experimental setup, we found two self-organized patterns in the confined actomyosin system. In the first pattern, the steady flow of actin filaments (F-actin) was continuously transported from the membrane boundary toward the center of the droplet, which we named “steady actin flow” [Fig. 1(c), Movie S1]. In the second pattern, the F-actin formed a ring-shaped pattern, where a gel-like structure was periodically formed at the periphery of the droplet and moved toward the center, which we named “actin waves” [Fig. 1(d), Movie S2]. Both patterns share the characteristic behavior of F-actin being transported toward the center of the droplet. However, in the steady actin flow pattern, the F-actin density was constant over time, whereas in the periodic actin wave pattern, the actin density periodically changed due to the periodic contraction of the actin gel toward the center [Figs. 1(e)–1(g)]. Elucidating the physical and molecular processes that cause these distinct

F-actin density dynamics is key to understanding the mechanism of pattern formation in the confined actomyosin system.

In theoretical models of actomyosin systems, contractile stress has been proposed as a primary factor that breaks translational symmetry [16–18]. To examine the influence of contractile stress on the observed self-organized patterns of actomyosin networks, we added Calyculin A (hereafter called “CalA”), a myosin II phosphatase inhibitor, resulting in increased contractile stress. By increasing the concentration of CalA, we observed a state transition from a steady actin flow to ring-shaped periodic actin waves [Fig. 1(h)]. These patterns can be clearly distinguished in the angular kymographs extracted from the time-lapse images [Figs. 1(e)–1(g)]. If F-actin is continuously contracting in the case of steady actin flow, visually identifying the steady actin flow in the kymograph would be difficult. To show the presence of steady actin flow, we added velocity vectors of steady actin flow calculated using particle image velocimetry on F-actin fluorescence [Fig. 1(c)].

To quantitatively characterize the state transition, we averaged the fluorescence intensity of F-actin over the angle $0 < \theta < 360$ (deg.) within the region of interest ($0.45R < r < 0.55R$, where r is the distance from the droplet center, and R is the radius of the droplet), and periodic structures were detected using Fourier transform (Fig. S1, Methods) [27]. In the power spectrum of the fluorescence intensity of F-actin, the peak frequency $1/T \rightarrow 0$ indicates the wave period of $T \rightarrow \infty$, corresponding to the steady actin flow. In contrast, the finite peak frequency $1/T$ corresponds to the periodic actin waves with a finite wave period T . It is notable that the periodic actin waves emerge at CalA concentrations greater than 30 μM [Fig. 1(h)]. The wave period mostly remained at the same value $T \simeq 1.5$ min for the high CalA concentration, indicating that the period is not primarily determined by the myosin contractility but by other factors such as actin polymerization dynamics [22].

B. Contractility and polymerization rate control the state transition

To elucidate the critical molecular determinants involved in the transition from steady actin flow to periodic actin waves, we performed molecular perturbations to change the contractility and polymerization rate. Under control conditions, the steady actin flow was stable [Figs. 2(a) and 2(b), (i)]. After increasing the contractility with CalA, periodic actin waves emerged [Figs. 2(a) and 2(b), (ii)], and the steady actin flow emerged again by increasing the polymerization rate of F-actin by adding the VVCA (Verprolin, cofilin, acidic) domain of N-WASP, which activates the Arp2/3-mediated actin polymerization [Figs. 2(a) and 2(b), (iii), Movie S3]. Conversely, the steady actin flow in the control condition was transformed into periodic actin waves by decreasing the F-actin polymerization rate with the addition of Cytochalasin D, an inhibitor of F-actin polymerization [Figs. 2(a) and 2(b), (iv), Movie S4], and the steady actin flow emerged again by decreasing the contractility by adding the myosin phosphorylation inhibitor Y27632 [Figs. 2(a) and 2(b), (v), Movie S5].

We also attempted to inhibit specific F-actin nucleators, a branched F-actin nucleator Arp2/3 complex, and an un-

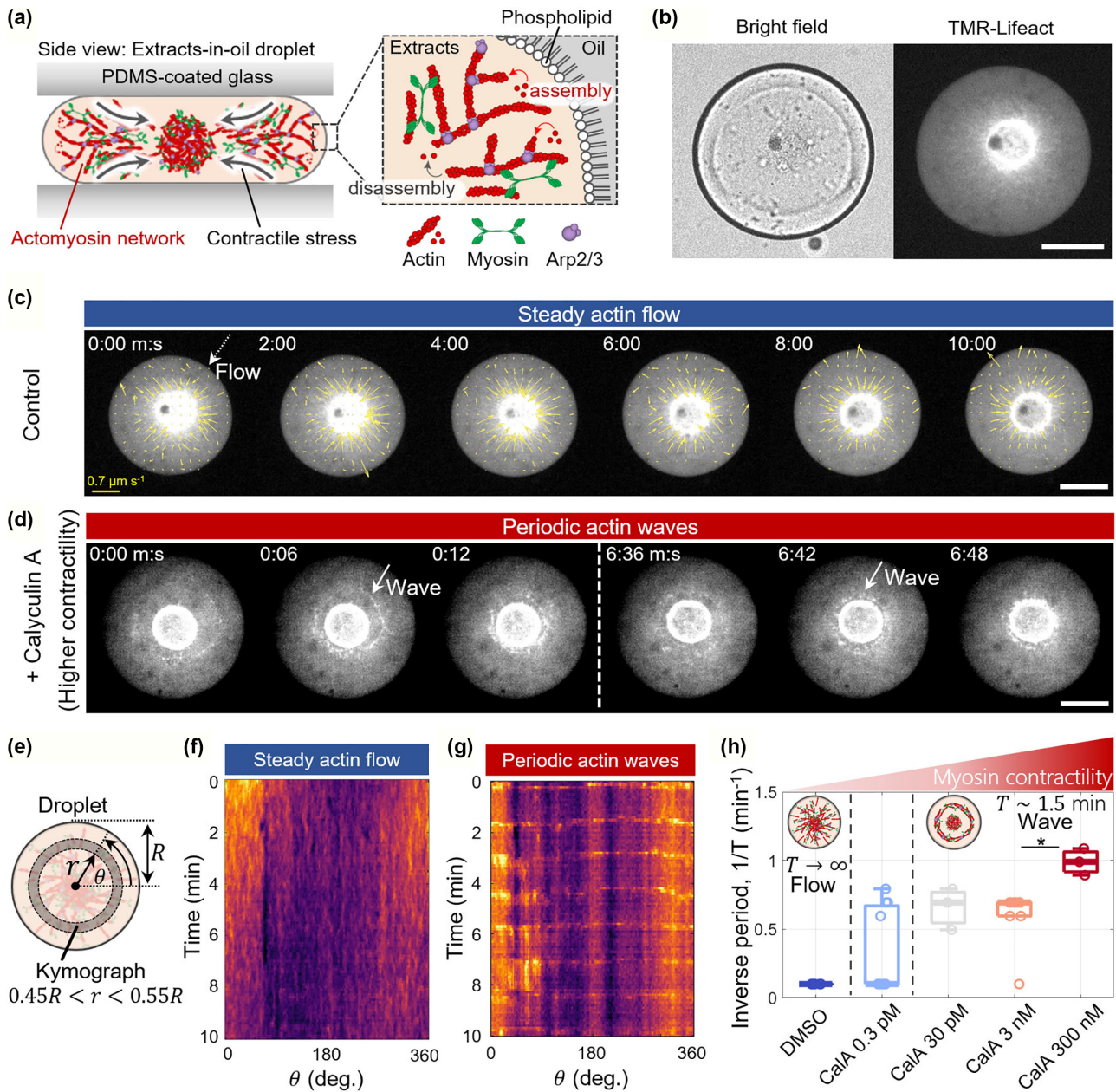


FIG. 1. Increased contractility induces the transition from the steady actin flow to the periodic actin waves. (a) Schematic showing the experimental setup. Droplets were confined between PDMS-coated glass slides, and the dynamics of the actomyosin contraction was observed by confocal microscopy. (b) A representative image captured at the middle plane of the droplet. (c) Time-lapse images showing the steady actin flow under a control condition. The velocity field was calculated using particle image velocimetry (PIV) and averaged for 2 min. (d) Time-lapse images showing the periodic actin wave contraction after adding 30 nM Calyculin A. (e) Schematic showing the definition of the region of interest (ROI) where kymograph was extracted for (f) and (g). (f) Angular kymograph extracted from (c). (g) Angular kymograph extracted from (d). Horizontal stripes are the ring-shaped actin waves. (h) The inverse period (frequency of the wave) was analyzed using the angular kymograph (Fig. S1). Wavelike structure emerged at the Calyculin A (CaIA) concentration larger than 0.3 pM. All images were captured by confocal microscopy. m:s stands for minutes and seconds. * stands for $p < 0.05$. Scale bars, 100 μm .

branched F-actin nucleator formin protein. First, by adding the Arp2/3 inhibitor CK666, periodic actin waves emerged; this result is similar to those of Cytochalasin D (Fig. S2). The period of actin waves slowed with the addition of CK666, suggesting the contribution of Arp2/3-mediated F-actin polymerization, consistent with our previous study [22]. In contrast, with the addition of the formin inhibitor SMIFH2, neither steady actin flow nor periodic actin waves emerged

(Fig. S2). Note that SMIFH2 did not specifically suppress formin in the present extracts, but it also substantially inhibited the ATPase activity of several myosin types [28]. Thus, we speculate that observing no apparent contraction upon the addition of SMIFH2 might be due to the inhibition of myosin contractility. As we could not specify the molecular target of SMIFH2 inhibition, we chose CK666 to confirm the contribution of the F-actin nucleator in this study.

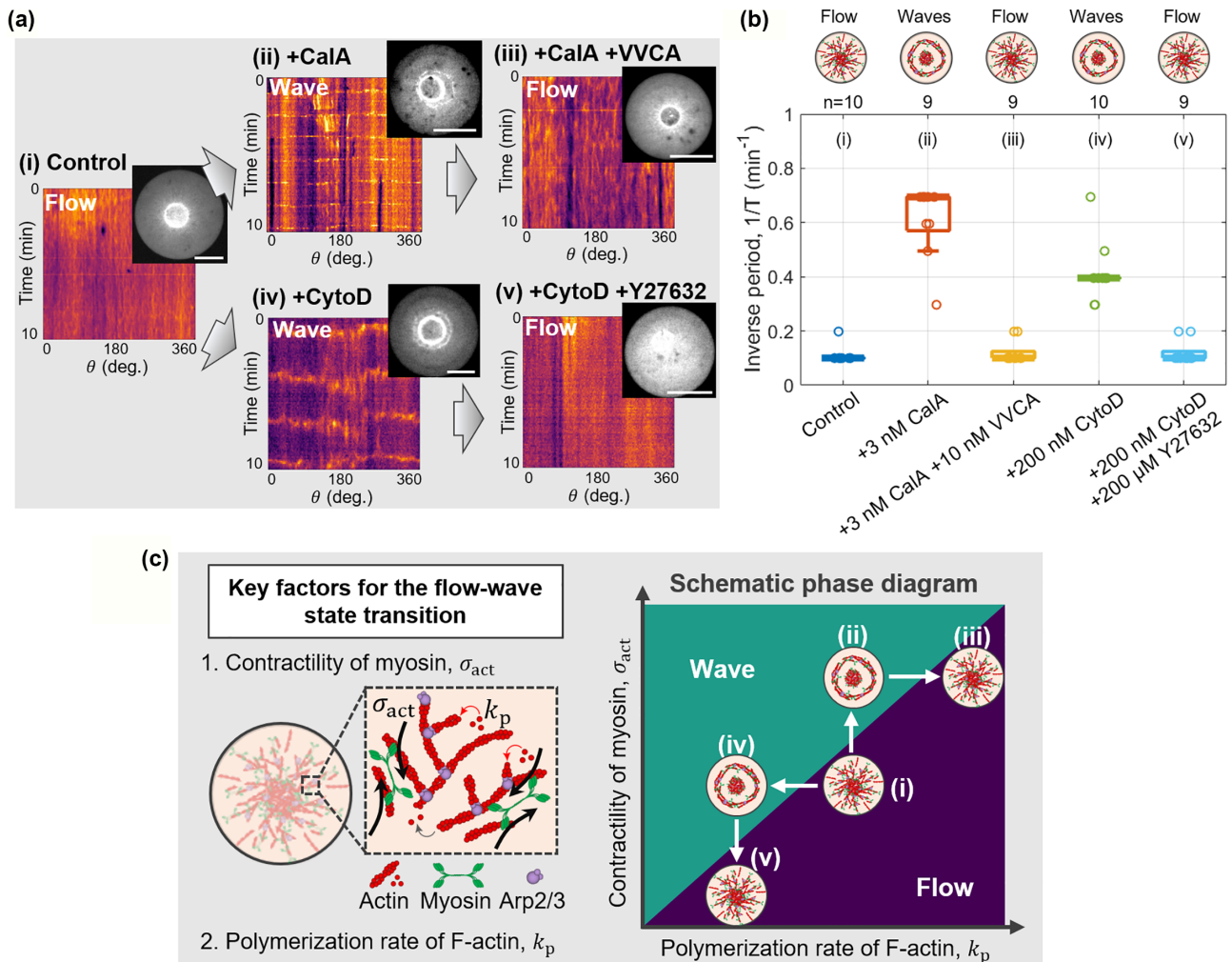


FIG. 2. (a) Transition between flow and wave was experimentally confirmed by the molecular perturbations. (i) Control condition. (ii) By adding Calyculin A, a myosin phosphatase inhibitor, the contractility of myosin σ_{act} was increased, and the actin wave state was stabilized. (iii) By adding the VVCA, an activator of actin nucleator Arp2/3, the polymerization rate k_p increased, and the flow state was stabilized. (iv) By adding Cytochalasin D, an F-actin polymerization inhibitor, the polymerization rate k_p was decreased, and the actin wave state was stabilized. (v) By adding the Y27632, an inhibitor of myosin phosphorylation, the contractility was decreased, and the flow state was stabilized. (b) Wave periods calculated from Fourier transformation of the intensity profiles in (a). (c) Conceptual model and schematic phase diagram. Flow-to-wave transition is controlled through (1) contractility of myosin σ_{act} and (2) polymerization rate of F-actin k_p . The right panel summarizes the schematic phase diagram inferred from the molecular perturbations. All images were captured by confocal microscopy. Scale bars, 100 μm .

Conclusively, these molecular perturbations revealed that myosin contractility and F-actin polymerization are keys to controlling the state transition between the steady actin flow and periodic actin waves [Fig. 2(c)].

C. Active fluid model of contractile actomyosin networks

To understand the physical mechanism of the transition from steady actin flow to periodic actin waves, we developed a theoretical model of contractile actomyosin networks confined in quasi-2D circular confinement [Fig. 3(a)]. We described the actomyosin networks as an active fluid producing active stress σ_{act} , which experiences the internal viscous stress σ_{vis} and external friction from the cytoplasm and the membrane $-\gamma\mathbf{v}$, where γ is the effective friction coefficient and \mathbf{v} is the velocity of the actomyosin gel [17,18].

Thus, the momentum balance for the active fluid is given by

$$\nabla \cdot (\sigma_{\text{vis}} + \sigma_{\text{act}}) = \gamma\mathbf{v}. \quad (1)$$

The viscous stress is given by the dissipative part of the viscous fluid [29]:

$$\sigma_{\text{vis}} = \eta[\nabla\mathbf{v} + (\nabla\mathbf{v})^T] + \eta_b(\nabla \cdot \mathbf{v})\mathbf{I}, \quad (2)$$

where η and η_b are the dynamic and bulk viscosities, respectively, and \mathbf{I} is the identity matrix. Additionally, the active stress was assumed to be proportional to the density of the actomyosin gel,

$$\sigma_{\text{act}} = (\zeta \Delta\mu)_0 f(\rho)\mathbf{I}, \quad (3)$$

where $(\zeta \Delta\mu)_0$ is the effective myosin contractile stress per F-actin, ρ is the local density of actomyosin gel, and $f(\rho) =$

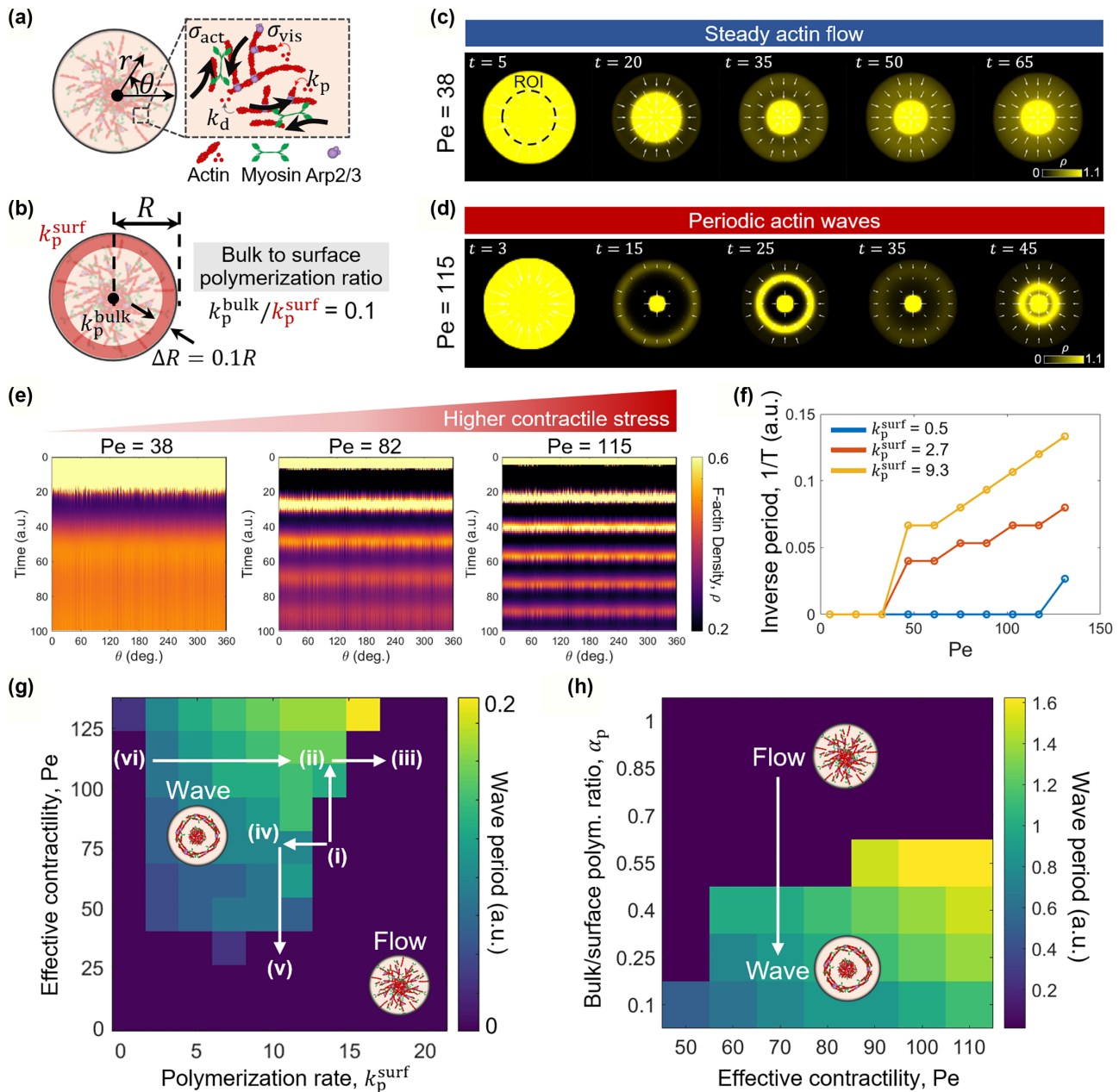


FIG. 3. Active fluid model of the steady actin flow to ring-shaped wave transition. (a) Schematic showing the internally generated active stress σ_{act} , viscous stress σ_{vis} , and polymerization and depolymerization rate of F-actin k_p and k_d , respectively. (b) Schematic showing the definition of bulk and surface polymerization rate k_p^{bulk} and k_p^{surf} , respectively. Here, we assume that the surface polymerization rate is 10 times faster than the bulk polymerization rate to mimic the experimentally observed local F-actin polymerization at the inner droplet surface. (c) At the Péclet number $Pe = 38$, steady actin flow emerged. White arrows indicate the velocity field. (d) At $Pe = 115$, periodic actin waves emerged. (e) Angular kymographs were extracted from the ROI in the time sequences (c) and (d). The larger the Péclet number (i.e., effective contractility), the more the periodic actin waves stably emerged. (f) Péclet number dependence of the peak frequency is shown. The graph shows that the periodic waves emerged at a certain Pe as the Pe increased. (g) Phase diagram of the active fluid model by changing the Pe and k_p^{surf} . (h) Phase diagram of the active fluid model by changing the bulk-to-surface polymerization ratio α_p .

$\rho/(\rho_0 + \rho)$, where ρ_0 is a constant [17,18]. For simplicity, we assumed that local myosin density is proportional to F-actin density [18]. Thus, we considered only the mass conservation equation for F-actin:

$$\frac{\partial \rho}{\partial t} + \nabla \cdot (\rho \mathbf{v}) = D \nabla^2 \rho + k_p - k_d \rho, \quad (4)$$

where D is the effective diffusion constant of F-actin, and k_p and k_d are the polymerization and depolymerization rates of F-actin, respectively. For simplicity, the orientation of F-actin was assumed not to play a substantial role in the state transition behaviors in this study. Previous studies using *Xenopus* egg extracts have also used isotropic models that reproduced the contractile behavior of the cytoplasmic actomyosin network [22,24].

D. Numerical simulation in a 2D circular domain imposed by a phase-field model

To implement a quasi-2D circular confinement mimicking extracts-in-oil droplets, we used a phase-field model [29–33]. Specifically, we used the phase-field dynamics developed in [29], which is expressed as

$$\frac{\partial \phi}{\partial t} = D_\phi \nabla^2 \phi + \Gamma_\phi U'(\phi). \quad (5)$$

The first term on the right side describes the resistance to the deformation, where the parameter D_ϕ has a similar effect to surface tension [29,31]. The second term is introduced to conserve droplet volume, and U' is the derivative of the double-well potential U , $U'(\phi) = \phi(\phi - 1)[\phi - 1/2 - \alpha_0(V/V_{\text{tar}} - 1)]$, where the fixed points $\phi = 0$ and 1 describe the outside and inside of the droplet, respectively. The term $\alpha_0(V/V_{\text{tar}} - 1)$ describes the conservation of droplet volume $V = \iint d\mathbf{r} \phi$ toward a target volume V_{tar} . The parameter α_0 characterizes the stiffness of this constraint [31]. The ratio of parameters $(8D_\phi/\Gamma_\phi)^{1/2}$ determines the characteristic width of the droplet boundary [29]. As we were interested in the actomyosin dynamics in circular confinement, we imposed an immobile nondeformable boundary condition by eliminating the advection term $-\mathbf{v} \cdot \nabla \phi$ [29]. We also neglected the bending rigidity of the membrane for the current purpose, which corresponds to higher-order differentials in ϕ [30,32,33].

In the present phase-field model, the no-flux boundary condition on actomyosin gel was imposed by an effective energy $E(\rho, \phi) = \iint d\mathbf{r} \{(\rho^2 + \beta)(1 - \phi)^2 + \beta\}^{1/2}$, which is an addition to the chemical potential of actomyosin gel, and β was introduced to avoid singularities [29]. This led to the final, full set of nondimensionalized equations:

$$\nabla^2 \mathbf{v} + \lambda \nabla(\nabla \cdot \mathbf{v}) + \nabla f = \mathbf{v}, \quad (6)$$

$$\frac{\partial \rho}{\partial t} + \text{Pe} \nabla \cdot (\rho \mathbf{v}) = \nabla^2 \rho + k_p - k_d \rho + \epsilon_\rho \nabla^2 \frac{\delta E}{\delta \rho}, \quad (7)$$

$$\frac{\partial \phi}{\partial t} = D_\phi \nabla^2 \phi + \Gamma_\phi U'(\phi), \quad (8)$$

where the lengthscales and timescales were nondimensionalized by the lengthscales unit $l = (\eta/\gamma)^{1/2}$ and the timescale unit $\tau = \eta/D\gamma$. The Péclet number (i.e., the ratio between the timescale of advective and diffusive transport) is defined as $\text{Pe} = Cl/D = (\zeta \Delta \mu)_0/D\gamma$, where the characteristic velocity $C = (\zeta \Delta \mu)_0/(\eta\gamma)^{1/2}$ is introduced. The rescaled parameters were redefined as $\rho/\rho_0 \rightarrow \rho$, $k_p/\rho_0\tau \rightarrow k_p$, $k_d/\tau \rightarrow k_d$. We assumed the constant $\lambda = 1 + \eta_p/\eta = 1/3$ to simplify the momentum balance equation [29]. The explicit form of the functional derivative in Eq. (7) is $\delta E/\delta \rho = \rho\{(\rho^2 + \beta)^{-1}[(1 - \phi)^2 + \beta]\}^{1/2}$. Additionally, we assumed that the local actin polymerization near the inner surface of the droplet was faster than that in the bulk space within the droplet. This assumption is based on previous experimental observations. Although the exact mechanism remains uncertain, studies have reported the local polymerization of F-actin at the periphery of the droplet when extracts were confined to water-in-oil droplets [20,22]. It has been reported that the VCA domain of WASP can be adsorbed onto the extracts-oil interface due to its partially hydrophobic nature, by which

the local actin assembly may be activated [34]. Here, we defined the bulk-to-surface ratio of the polymerization rate as $\alpha_p \equiv k_p^{\text{bulk}}/k_p^{\text{surf}} = 0.1$, where k_p^{bulk} is the bulk polymerization rate at $0 < r < 0.9R$, and k_p^{surf} is the surface polymerization rate at $0.9R < r < R$ [Fig. 3(b)].

First, we present the numerical results for $\text{Pe} = 38$, $k_p^{\text{surf}} = 1.5$, $k_d = 1$, $\beta = 0.0001$, $D_\phi = 1$, $\Gamma_\phi = 160D_\phi$, $\epsilon_\rho = 20$, $\alpha_0 = 50$ with the initial condition of $\rho(x, y) = 1$, $v(x, y) = 0$. At the boundary of the droplet, the uniform actomyosin networks started to contract inward, forming a high-density actomyosin cluster at the center of the circular domain [Figs. 3(c) and 3(d)]. Subsequently, steady actin flow emerged at $\text{Pe} = 38$ [Figs. 3(c) and 3(e), Movie S6], whereas the periodic actin waves emerged at $\text{Pe} = 115$ [Figs. 3(d) and 3(e), Movie S6]. Fourier analysis of the F-actin density ρ showed that periodic actin waves emerged as the Péclet number Pe increased [Fig. 3(f)], consistent with the experimental observations [Fig. 1(h)]. As the Péclet number is predominantly determined by the contractility when D and γ are fixed, this result indicates contractility-induced instability of the actomyosin system. The wave period was shorter for the higher surface polymerization rate k_p^{surf} [Fig. 3(f)], suggesting that F-actin polymerization determines the periodicity of actin waves, consistent with the experimental results (Fig. S2) [22].

The phase diagram was obtained by changing Pe and k_p^{surf} [Fig. 3(g)]. The phase diagram again showed that the periodic actin waves emerged as Pe increased [Fig. 3(g), (i)–(ii)]. Decreasing the polymerization rate also induces a flow-to-wave transition [Fig. 3(g), (i)–(iv)], and the simultaneous reduction of contractility leads to the flow [Fig. 3(g), (iv)–(v)], as observed in the experiments [Fig. 2(c)]. At a very low polymerization rate $k_p^{\text{surf}} \sim 0$, steady actin flow was stable [Fig. 3(g), (vi)]. Periodic actin waves emerged when the polymerization rate was increased toward $k_p^{\text{surf}} > 1$ [Fig. 3(g), (vi)–(ii)]. Notably, the steady actin flow stabilized again with a higher polymerization rate [Fig. 3(g), (ii)–(iii)], consistent with the experimental observations [Fig. 2(c)]. The reason for this might be that at a high polymerization rate, newly polymerized filaments are immediately transported toward the center of the droplet, by which the actomyosin density around the surface becomes smaller, thereby suppressing the formation of periodic actin waves. Thus, this result suggests that the higher actomyosin density in the vicinity of the droplet surface than in the bulk could be an important factor in generating periodic actin waves.

We fixed the bulk-to-surface polymerization ratio $\alpha_p = k_p^{\text{bulk}}/k_p^{\text{surf}} = 0.1$ to describe the local F-actin assembly at the droplet surface in our experiments [22]. However, as suggested by the reentrant transition from periodic actin waves to steady actin flow at a higher polymerization rate in the phase diagram [Fig. 3(g), (ii)–(iii)], the bulk-to-surface contrast of actomyosin density could affect the contractile behavior of the actomyosin system. To clarify the contribution of α_p , we altered the bulk-to-surface polymerization ratio to within $0.1 < \alpha_p < 1$ by changing k_p^{bulk} with a fixed k_p^{surf} [Fig. 3(h)]. Notably, at a fixed Pe , the periodic actin waves only emerged at a smaller bulk-to-surface polymerization ratio $\alpha_p < 0.5$ (i.e., a higher surface polymerization than the bulk), suggesting that the contrast of the bulk-to-surface

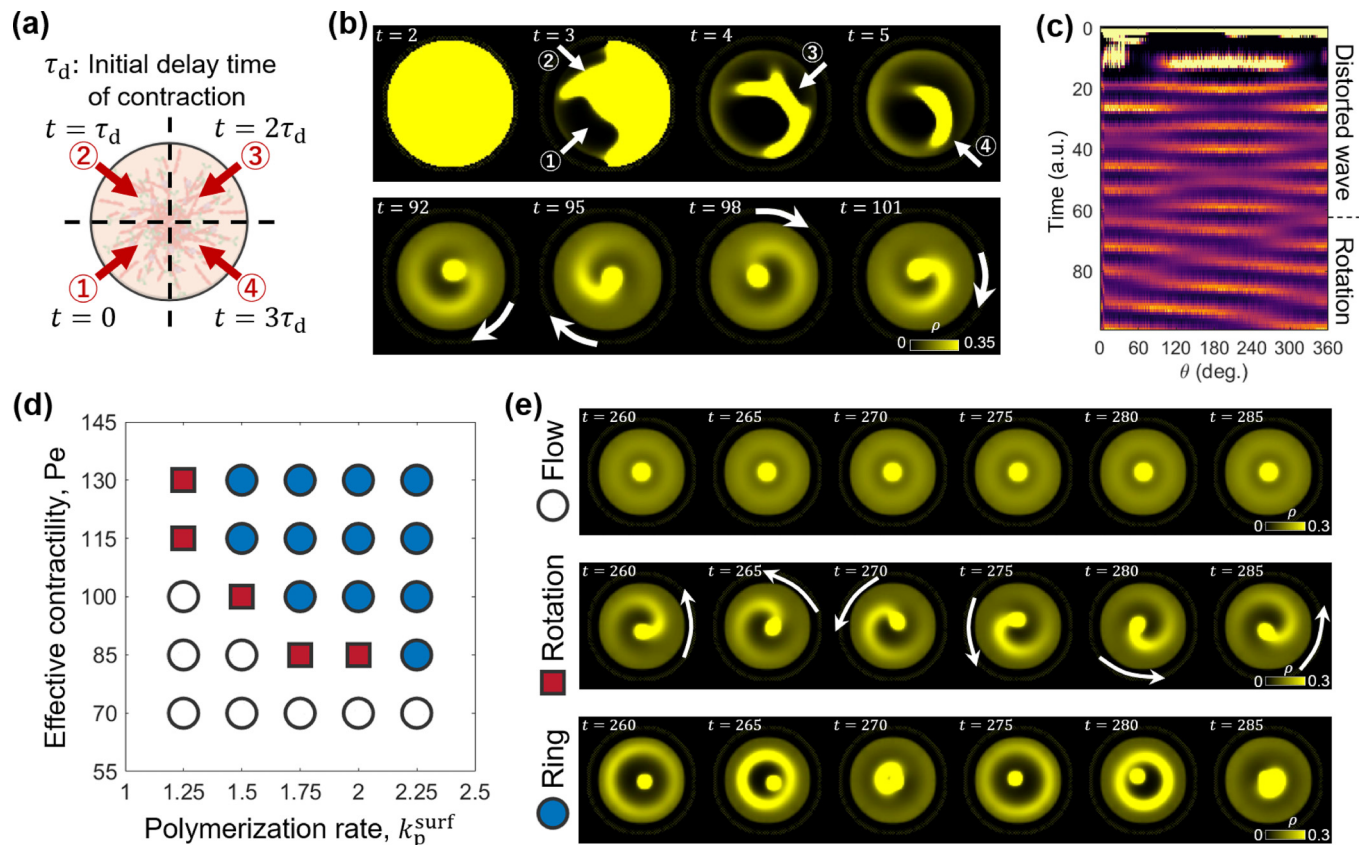


FIG. 4. Initial time delay of the contraction induces the rotational symmetry breaking. (a) Schematic showing the definition of the time delay in contraction. The circular domain was divided into four regions, in which each region successively starts to contract with time delay τ_d . (b) Time-lapse images of the initial time delay in contraction and the emergence of the rotational wave. Parameters were $Pe = 90$, $k_p^{\text{surf}} = 1.75$, and $\alpha_p = 0.01$. (c) Angular kymograph extracted from (b). (d) Phase diagram with the initial time delay in the contraction. Each symbol corresponds to the flow (empty circle), the wave (filled blue circle), and the rotation wave (filled red square). The simulation was performed with the bulk to surface polymerization ratio $\alpha_p = 0.01$. (e) Representative examples of distinct wave behaviors. Each image corresponds to $Pe = 85$, $k_p^{\text{surf}} = 1.5$ (flow, empty circle); $Pe = 100$, $k_p^{\text{surf}} = 1.5$ (rotation wave, filled red square); $Pe = 115$, $k_p^{\text{surf}} = 1.75$ (ring-shaped wave, filled blue circle).

polymerization rate crucially determines the contractile behavior of the confined active gels. Therefore, our active fluid model also predicts the phase transition of contractile behavior in terms of the ratio of the bulk-to-surface polymerization rate α_p .

E. Time delay of initial contraction-induced rotational symmetry breaking

Our theoretical model considered a uniform progression of actin polymerization at the membrane surface; however, the initiation of actin polymerization in cells and reconstituted systems often occurs heterogeneously. To test how such heterogeneity alters pattern formation, we performed numerical calculations with a nonuniform time delay in initiating actomyosin contraction at the surface. The nondeformable circular domain was divided into four regions, and each region initially started to contract with the time delay τ_d [Fig. 4(a)]. Specifically, at $t = 0$, we initiate the time evolution of Eqs. (6) and (7) in region 1, while the actomyosin density in regions 2–4 was kept as the initial value. Subsequently, at $t = \tau_d$ and after that, we allow the time evolution of regions 2–4. In this

way, we describe the time delay in the initiation of contraction (i.e., spatial heterogeneity of the initiation of contraction).

With the time delay $\tau_d = 10^{-2}T_s$ (T_s is the total simulation duration), we found that the rotational wave became stable after several time steps [Figs. 4(b) and 4(c), and Movie S7]. This suggests that an initial perturbation in the distribution of actomyosin networks can break the rotational symmetry. The phase diagram shows that with a fixed k_p^{surf} , the steady actin flow is stable at a small Pe , whereas this flow is destabilized at a large Pe and becomes ring-shaped periodic actin waves, as discussed [Figs. 4(d) and 4(e), Movie S8]. However, with the time delay of the initial contraction, a rotational wave emerged at the phase boundary between the steady actin flow and the periodic actin waves [Figs. 4(d) and 4(e), red squares, Movie S8].

The aforementioned results can be interpreted as follows: In our active fluid model, the contractile behavior of the actomyosin networks could be determined by a competition between the bulk actomyosin network located near the center of the droplet and the surface actomyosin network polymerized in the vicinity of the droplet periphery. The bulk actomyosin network self-organizes into steady actin flow, and the surface actomyosin network self-organizes into periodic

actin waves. By increasing the bulk polymerization rate, steady actin flow was observed in the larger phase space (Fig. S3). Thus, the rotational wave could emerge at the phase boundary between the steady actin flow and periodic actin waves, where the competing contractile forces between the bulk and surface actomyosin networks may be balanced. Importantly, we confirmed that the magnitude of τ_d did not affect the period of the finally stabilized rotational wave, indicating that the emergence of the rotational wave is independent of the initial condition; therefore, a self-organized stable state is determined by the physical parameters of the actomyosin system (Fig. S4). However, the detailed mechanisms remain unclear because of the difficulty in obtaining an analytical expression from complex equations with imposed boundary conditions. A detailed analysis, such as nonlinear perturbation analysis, can be explored in further research.

II. DISCUSSION

Previous studies using cytoplasmic actomyosin networks found various contractile behaviors of the actomyosin networks, such as steady actin flow [20,24] and ring-shaped periodic actin waves [21,22], whereas how these distinct contractile behaviors could emerge in the same actomyosin system has been elusive. In this study, by combining molecular perturbations and theoretical modeling of active gels, we showed that distinct contractile behaviors emerged in the same cytoplasmic actomyosin networks by fine tuning the contractility of myosin and the polymerization rate of F-actin, where we constructed a simple theoretical model explaining the mechanism of the transition between the distinct contractile behaviors from the steady actin flow to the ring-shaped periodic actin waves.

Recent experimental studies have shown that contractile actomyosin networks can be used to move large nucleuslike structures toward the center of extracts-in-oil droplets [22,25]. However, in these studies, different actomyosin structures, either the inward steady actin flow or the ring-shaped periodic actin waves, were separately proposed as driving forces for the centering of large nucleuslike structures. Based on this study, we can understand that such distinct self-organized actomyosin structures are not mutually exclusive but can be realized in the same actomyosin system depending on myosin contractility and the F-actin polymerization rate. Therefore, our study provides an integrative understanding of the self-organization of actomyosin networks confined to cell-sized spaces.

Theoretical studies have shown that the pattern formation in active gels is stabilized when the active stress outweighs the diffusive relaxation in 2D periodic systems [16–18] and in the surface of a sphere as a model of the cell cortex [35,36]. In this study, we demonstrated the importance of the combination of intracellular and cortical actomyosin networks within the cell-like closed spaces that can together drive state transitions, wherein both the strength of the active stress and the polymerization rate determine the stable states. Recent experimental studies have shown the importance of cytoplasmic actomyosin networks in cell division [12], spindle positioning [19], and cytoplasmic segregation [37]. Thus, the active fluid model developed in this study may provide mechanical

insights into contractile behaviors widely observed in living cells, highlighting the potential importance of the mechanics of intracellular actomyosin networks interacting with the actomyosin cortex.

Our confined active fluid model also predicted the emergence of rotational waves based on the time delay of the onset of contraction. Such a time delay could occur in living cells because the actomyosin network is tightly bound to the cell plasma membrane, and the onset of contraction could be spatially heterogeneous. Notably, theoretical works have predicted spontaneous rotational symmetry breaking of active fluids by considering the microscopic polarization field (orientation field) of F-actin [41–43]. When actin-binding lipids increase actin-membrane interactions in extracts-in-oil droplets, filament orientation at the water-oil interface might play a role in inducing rotational symmetry breaking, such as by changing the direction of the motion of migrating actomyosin droplets [26]. The experimental realization of rotational waves in extracts-in-oil droplets remains an important topic for future research.

Several experimental studies have reported rotational waves driven by contractile actomyosin networks in various cell types, including fibroblasts [10], HeLa cells [11], CHO cells [9], fish parasites [38], and *Xenopus* blastomeres [13]. This suggests that a rotational wave could be a universal biological phenomenon that is not considerably affected by the system details. In a biological context, rotational waves might be related to polarity formation at the onset of migration. The literature has revealed that increased contractility induces polarity formation in migratory cells, whereas some cells fail to form stable polarity and undergo rotational behaviors [39,40]. Thus, understanding the mechanism of rotational waves might also provide implications for polarity formation without entering into the rotational wave state. Moreover, during the cell division of epithelial cells, rotational actin waves were shown to randomize the mitochondrial position, increasing the probability that each daughter cell receives an equivalent amount of mitochondrial networks. This process may be necessary for epithelial regeneration to maintain tissue homeostasis [12].

Note that the confined space represented by the phase field is assumed to be immobile and nondeformable in this study. Although the no-flux boundary condition may be easily introduced in polar coordinates, we chose the phase-field model after considering a future extension toward mobile, deformable droplets. Our recent study reported deformable motile droplets encapsulating cytoplasmic actomyosin networks [26], and the present phase-field model is well-suited for describing these behaviors.

III. CONCLUSIONS

Confined actomyosin networks undergo state transitions between steady actin flow and periodic actin waves by tuning myosin contractility and the F-actin polymerization rate. Numerical simulations based on the mechanics of the actomyosin network explained these experimental observations and predicted a time-delay-induced rotational wave. These results indicate that the mechanics of actomyosin alone can control distinct patterns, highlighting the potential importance of

mechanics in the pattern formation of the confined actomyosin system in cells.

IV. MATERIALS AND METHODS

A. Preparation of *Xenopus* egg extracts

Actin-intact extracts were prepared as previously described [22]. First, actin-intact cytoplasmic extracts were prepared from *Xenopus laevis* eggs [21]. Immediately thereafter, a 1/1000 volume of protease inhibitors (10 mg mL⁻¹ leupeptin, 10 mg mL⁻¹ pepstatin A, 10 mg mL⁻¹ chymostatin dissolved in DMSO), a 1/20 volume of 2 M sucrose, and a 1/20 volume of energy mix (150 mM creatine phosphate, 20 mM ATP, and 20 mM MgCl₂) was added. The extracts were then divided into 20 μ L aliquots, snap-frozen in liquid nitrogen, and stored at -80°C .

B. Preparation of recombinant proteins

Recombinant proteins were prepared as previously described [22]. The VVCA domain of mouse N-WASP cDNA (385–501 aa) was cloned into the pGEX-6P vector (Cytiva) and expressed in *E. coli*. (Rosetta2(DE3), Merck Millipore) at 37°C for 3 h in the presence of 1 mM IPTG. GST-tagged VVCA was purified on a GSTrap HP column (Cytiva), followed by dialysis against A50 buffer (50 mM HEPES-KOH pH7.6, 50 mM KCl, 5 mM MgCl₂, and 1 mM EGTA) containing 1 mM DTT at 4°C . The sample was further purified using a size exclusion column (Superdex 200 Increase 10/300 GL, Cytiva) with A50 buffer containing 1 mM DTT; snap-frozen in liquid nitrogen; and stored at -80°C . Protein concentration was determined using a Protein Assay Kit (500-0006, Bio-Rad), with a molecular weight of 39 500 Da.

C. Preparation of PDMS-coated glass slides

Glass slides were coated with a silicone elastomer (polydimethylsiloxane, PDMS) (Sylgard 184; Dow Corning) as previously described [22]. Uncured PDMS mixed with a curing agent was poured onto the glass slides, and then PDMS was spread using a spin coater (1000 rpm, 20 s). The PDMS-coated glass slides were cured for 1 h at 75°C . PDMS-coated coverslips ($18 \times 18 \text{ mm}^2$) were prepared by cutting the PDMS-coated glass with a glass cutter.

D. Encapsulation of extracts in droplets

Droplets were generated as previously described [22]. First, an aliquot of the extract (20 μ L) frozen at -84°C was thawed and then incubated on ice for 1 h. Thereafter, 0.2 μ L TMR-Lifeact dissolved in dimethyl sulfoxide (DMSO) (final 1 μ M) and 0.2 μ L nocodazole dissolved in DMSO (final 100 μ M) were added to the extracts. To prepare the control condition as a steady actin flow state, we added 1 μ L of A50 buffer to slightly dilute the extracts. Simultaneously, 0.2 μ L Calyculin A, Cytochalasin D, and VVCA were added to the extracts for molecular perturbation. Note that both Cytochalasin D [20,22] and Latrunculin B [44] have been shown to effectively inhibit F-actin polymerization in *Xenopus* egg extracts. Furthermore, 0.4 μ L of the extract was injected into 14 μ L of a lipid-oil mixture [1 mM L- α -phosphatidyl choline from egg yolk (eggPC) (27554-01; Nacalai Tesque) in mineral oil (M5904; Sigma-Aldrich)] to produce steady actin flow

and ring-shaped periodic actin waves. By tapping the sample tube with a finger, we obtained a polydisperse emulsion of extract-in-oil. Immediately after emulsification, 3–7 μ L of the emulsion was placed on a PDMS-coated glass slide and gently covered with a PDMS-coated coverslip. The chamber height $h = 60 \mu\text{m}$ was controlled by the spacer thickness. For the molecular perturbation experiments in Fig. S2 of the Supplemental Material, we used the inhibitors at the final concentration of 1 mM CK666, 25 μ M SMIFH2, 100 μ M Cytochalasin D, and 1 mM Y27632.

E. Image analysis

Quantitative image analysis was performed using a custom code implemented in MATLAB. To quantitatively analyze the period of the contractile wave, we used Fourier analysis of the total intensity within the region of interest. Because the center of the droplet is the origin $r = 0$ in polar coordinates, the local density of the actin filaments was measured using local fluorescence intensity $I(r, \theta, t)$. The intensity was then averaged over the region of interest $0.45R < r < 0.55R$ and $0 < \theta < 2\pi$; thus, $I(t) \equiv \int_{0.45R}^{0.55R} \int_0^{2\pi} I(r, \theta, t) dr d\theta$. We then performed the Fourier transform $\bar{I}(\omega) = (1/2\pi) \int_0^{10\text{min}} I(t) e^{-i\omega t} dt$. Next, the period of the actin wave was calculated from the peak of $\bar{I}(\omega_{\text{peak}})$ using the relation $T_{\text{peak}} = 2\pi/\omega_{\text{peak}}$. Notably, $T_{\text{peak}} \rightarrow \infty$ (i.e., $\omega_{\text{peak}} \rightarrow 0$) corresponds to stationary flow, in which there is no oscillatory structure in the intensity time course. Notably, the $1/T$ calculated in Fig. 1(h) is slightly larger than zero. This occurs because the decrease in fluorescence intensity by photobleaching was detected as a low-frequency signal with a small $1/T$ value via Fourier analysis. Nevertheless, we can clearly distinguish steady flow from waves because the wave period has a much higher frequency than the background signal. Additionally, to visualize the spatial velocity profile of actin flow [Fig. 1(c)], we used a public domain particle image velocimetry (PIV) program implemented as a Fiji ImageJ plugin.

F. Microscopy

To visualize the F-actin network in detail, we used confocal microscopy and focused on the midplane of the confined droplet. Time-lapse images of steady actin flow and periodic actin waves were acquired every 6 s using a confocal microscope (IX73; Olympus) and confocal scanning unit (CSU-X1; Yokogawa Electric Cor. Ltd.) equipped with an iXon-Ultra EM-CCD camera (Andor Technologies) and $\times 20$ objective lens (UPlanSApo 20 \times /0.75; OLYMPUS) under a 561 nm fluorescence channel. Time-lapse images of rotational waves were acquired every 6 s using a microscope (IX73; Olympus) equipped with a $\times 20$ objective lens (TU Plan ELWD 20 \times /0.40; Nikon), cooled CMOS camera (Neo5.5; Andor Technology), and stable excitation light source (XLED1; Lumen Dynamics). For all microscopic examinations, room temperature was maintained at $20 \pm 1^{\circ}\text{C}$.

G. Numerical simulation scheme

To solve our equations, we discretized them using a finite-difference method and performed numerical simulations. In each time step, we first determined the density and phase fields using Eqs. (7) and (8). We then updated the velocity

field by using the force balance in Eq. (6), which was solved using a spectral method. In all simulations, we used $\Delta x = 10^{-1}$, $\Delta y = 10^{-1}$, and $\Delta t = 10^{-5}$. We verified that our results did not change for smaller values.

For the simulation of rotational waves, we attempted a random initial condition such as adding small perturbation in the velocity and the density field; however, it was insufficient to realize the rotational symmetry breaking. This may have occurred because the spatial range of perturbation was too small for the system size, as rotational symmetry breaking is system-wide. Thus, we attempted to impose a system-wide perturbation, that is, a time delay in the initial contraction.

ACKNOWLEDGMENTS

We thank Y. Shimamoto for sharing materials. We would like to thank Editage [45] for English language editing. This work was supported by Grant-in-Aid for Scientific Research

(B) (Grant No. 20H01872 to Y.T.M.), Grant-in-Aid for Scientific Research on Innovative Areas “Molecular Engines” (Grant No. 18H05427 to Y.T.M., Grant No. 19H05393 to M.M.), JSPS Fellows (Grant No. JP19J20035 to R.S.), Grant-in-Aid for Challenging Research (Exploratory) (Grant No. 21K18605 to Y.T.M.) from the Ministry of Education, Culture, Sports, Science, and Technology, Japan, Human Frontier Science Program Research Grant (Grant No. RGP0037/2015 to Y.T.M.), Grant for Basic Science Research Project from The Sumitomo Foundation (to Y.T.M.). The Hakubi project of Kyoto University (to M.M.). JST PRESTO, Japan (Grant No. JPMJPR20ED to M.M.). Overseas Postdoctoral Fellowships of the Uehara Memorial Foundation (to R.S.).

R.S. and Y.T.M. designed research; R.S. performed experiments and analyzed data; R.S., M.M., and Y.T.M. contributed new reagents/analytic tools; R.S. constructed theoretical models and performed simulations; and R.S. and Y.T.M. wrote the paper.

There are no conflicts of interest to declare.

-
- [1] S. Kondo and T. Miura, Reaction-diffusion model as a framework for understanding biological pattern formation, *Science* **329**, 1616 (2010).
- [2] D. M. Raskin and P. A. de Borer, Rapid pole-to-pole oscillation of a protein required for directing division to the middle of *Escherichia coli*, *Proc. Natl. Acad. Sci. USA* **96**, 4971 (1999).
- [3] D. M. Raskin and P. A. de Borer, MinDE-dependent pole-to-pole oscillation of division inhibitor MinC in *Escherichia coli*, *J. Bacteriol.* **181**, 6419 (1999).
- [4] L. Marcon, X. Diego, J. Sharpe, and P. Möller, High-throughput mathematical analysis identifies Turing networks for patterning with equally diffusing signals, *eLife* **5**, e14022 (2016).
- [5] S. Köhler, V. Schaller, and A. Bausch, Structure formation in active networks, *Nat. Mater.* **10**, 462 (2011).
- [6] D. V. Köster, K. Husain, E. Iljazi, A. Bhat, P. Bieling, R. D. Mullins, M. Rao, and S. Mayor, Actomyosin dynamics drive local membrane component organization in an in vitro active composite layer, *Proc. Natl. Acad. Sci. USA* **113**, E1645 (2016).
- [7] T. H. Tan, M. Malik-Garbi, E. Abu-Shah, J. Li, A. Sharma, F. C. MacKintosh, K. Keren, C. F. Schmidt, and N. Fakhri, Self-organized stress patterns drive state transitions in actin cortices, *Sci. Adv.* **4**, eaar2847 (2018).
- [8] V. Wollrab, J. M. Belmonte, L. Baldauf, M. Leptin, F. Nédélec, and G. H. Koenderink, Polarity sorting drives remodeling of actin-myosin networks, *J. Cell Sci.* **132**, jcs219717 (2018).
- [9] Y. H. Tee *et al.*, Cellular chirality arising from the self-organization of the actin cytoskeleton, *Nat. Cell Biol.* **17**, 445 (2015).
- [10] M. K. Driscoll, W. Losert, K. Jacobson, and M. Kapustina, Spatiotemporal relationships between the cell shape and the actomyosin cortex of periodically protruding cells, *Cytoskeleton* **72**, 268 (2015).
- [11] M. Mitsushima, K. Aoki, M. Ebisuya, S. Matsumura, T. Yamamoto, M. Matsuda, F. Toyoshima, and E. Nishida, Revolving movement of a dynamic cluster of actin filaments during mitosis, *J. Cell Biol.* **191**, 453 (2010).
- [12] A. S. Moore *et al.*, Actin cables and comet tails organize mitochondrial networks in mitosis, *Nature (London)* **591**, 659 (2021).
- [13] G. T. Charras, M. Coughlin, T. J. Mitchison, and L. Mahadevan, Life and times of a cellular bleb, *Biophys. J.* **94**, 1836 (2008).
- [14] W. M. Bement *et al.*, Activator-inhibitor coupling between Rho signalling and actin assembly makes the cell cortex an excitable medium, *Nat. Cell Biol.* **17**, 1471 (2015).
- [15] J. Landino *et al.*, Rho and F-actin self-organize within an artificial cell cortex, *Curr. Biol.* **31**, 5613 (2021).
- [16] J. S. Bois, F. Jülicher, and S. W. Grill, Pattern Formation in Active Fluids, *Phys. Rev. Lett.* **106**, 028103 (2011).
- [17] K. V. Kumar, J. S. Bois, F. Jülicher, and S. W. Grill, Pulsatory Patterns in Active Fluids, *Phys. Rev. Lett.* **112**, 208101 (2014).
- [18] T. Moore, S. K. Wu, M. Michael, A. S. Yap, G. A. Gomez, and Z. Neufeld, Self-organizing actomyosin patterns on the cell cortex at epithelial cell-cell junctions, *Biophys. J.* **107**, 2652 (2014).
- [19] K. Yi *et al.*, Sequential actin-based pushing forces drive meiosis I chromosome migration and symmetry breaking in oocytes, *J. Cell Biol.* **200**, 567 (2013).
- [20] M. Pinot, V. Steiner, B. Dehapiot, B.-K. Yoo, F. Chesnel, L. Blanchoin, C. Kervrann, and Z. Gueroui, Confinement induces actin flow in a meiotic cytoplasm, *Proc. Natl. Acad. Sci. USA* **109**, 11705 (2012).
- [21] C. M. Field, M. Wühr, G. A. Anderson, H. Y. Kueh, D. Strickland, and T. J. Mitchison, Actin behavior in bulk cytoplasm is cell cycle regulated in early vertebrate embryos, *J. Cell Sci.* **124**, 2086 (2011).
- [22] R. Sakamoto, M. Tanabe, T. Hiraiwa, K. Suzuki, S. Ishiwata, Y. T. Maeda, and M. Miyazaki, Tug-of-war between actomyosin-driven antagonistic forces determines the positioning symmetry in cell-sized confinement, *Nat. Commun.* **11**, 3063 (2020).
- [23] E. A. Shah and K. Keren, Symmetry breaking in reconstituted actin cortices, *eLife* **3**, e01433 (2014).

- [24] M. Malik-Garbi, N. Ierushalmi, S. Jansen, E. Abu-Shah, B. L. Goode, A. Mogilner, and K. Keren, Scaling behaviour in steady-state contracting actomyosin networks, *Nat. Phys.* **15**, 509 (2019).
- [25] N. Ierushalmi, M. Malik-Garbi, A. Manhart, E. A. Shah, B. L. Goode, A. Mogilner, and K. Keren, Centering and symmetry breaking in confined contracting actomyosin networks, *eLife* **9**, e55368 (2020).
- [26] R. Sakamoto, Z. Izri, Y. Shimamoto, M. Miyazaki, and Y. T. Maeda, Geometric trade-off between contractile force and viscous drag determines the actomyosin-based motility of a cell-sized droplet, *Proc. Natl. Acad. Sci. USA* **119**, e2121147119 (2022).
- [27] See Supplemental Material at <http://link.aps.org/supplemental/10.1103/PhysRevResearch.5.013208> for details on the analysis methods.
- [28] Y. Nishimura, S. Shi, F. Zhang, R. Liu, Y. Takagi, A. D. Bershadsky, V. Viasnoff, and J. R. Sellers, The formin inhibitor SMIFH2 inhibits members of the myosin superfamily, *J. Cell Sci.* **134**, jcs253708 (2021).
- [29] T. L. Goff, B. Liebchen, and D. Marenduzzo, Actomyosin contraction induces in-bulk motility of cells and droplets, *Biophys. J.* **119**, 1025 (2020).
- [30] D. Shao, W. J. Rappel, and H. Levine, Computational Model for Cell Morphodynamics, *Phys. Rev. Lett.* **105**, 108104 (2010).
- [31] F. Ziebert, S. Swaminathan, and I. S. Aranson, Model for self-polarization and motility of keratocyte fragments, *J. R. Soc. Interface* **9**, 1084 (2012).
- [32] B. A. Camley, Y. Zhao, B. Li, H. Levine, and W.-J. Rappel, Periodic Migration in a Physical Model of Cells on Micropatterns, *Phys. Rev. Lett.* **111**, 158102 (2013).
- [33] B. A. Camley *et al.*, Polarity mechanisms such as contact inhibition of locomotion regulate persistent rotational motion of mammalian cells on micropatterns, *Proc. Natl. Acad. Sci. USA* **111**, 14770 (2014).
- [34] H. Boukellal, O. Campás, J.-F. Joanny, J. Prost, and C. Sykes, Soft Listeria: actin-based propulsion of liquid drops, *Phys. Rev. E* **69**, 061906 (2004).
- [35] A. Mietke, V. Jemseena, K. V. Kumar, I. F. Sbalzarini, and F. Jülicher, Minimal Model of Cellular Symmetry Breaking, *Phys. Rev. Lett.* **123**, 188101 (2019).
- [36] M. Bonati, L. D. Wittwer, S. Aland, and E. Fischer-Friedrich, On the role of mechanosensitive binding dynamics in the pattern formation of active surfaces, *New J. Phys.* **24**, 073044 (2022).
- [37] S. Shamipour *et al.*, Bulk actin dynamics drive phase segregation in zebrafish oocytes, *Cell* **177**, 1463 (2019).
- [38] G. Alama-Bermejo, A. S. Holzer, and J. L. Bartholomew, Myxozoan adhesion and virulence: ceratona shasta on the move, *Microorganisms* **7**, 397 (2019).
- [39] V. Ruprecht *et al.*, Cortical contractility triggers a stochastic switch to fast amoeboid cell motility, *Cell* **160**, 673 (2015).
- [40] V. Venturini *et al.*, The nucleus measures shape changes for cellular proprioception to control dynamic cell behavior, *Science* **370**, eaba2644 (2020).
- [41] A. Kumar, A. Maitra, M. Sumit, S. Ramaswamy, and G. V. Shivashankar, Actomyosin contractility rotates the cell nucleus, *Sci. Rep.* **4**, 3781 (2014).
- [42] E. Tjhung, D. Marenduzzo, and M. E. Cates, Spontaneous symmetry breaking in active droplets provides a generic route to motility, *Proc. Natl. Acad. Sci. USA* **109**, 12381 (2012).
- [43] E. Tjhung, M. E. Cates, and D. Marenduzzo, Contractile and chiral activities codetermine the helicity of swimming droplet trajectories, *Proc. Natl. Acad. Sci. USA* **114**, 4631 (2017).
- [44] M. T. Valentine, Z. E. Perlman, T. J. Mitchison, and D. A. Weitz, Mechanical properties of *Xenopus* egg cytoplasmic extracts, *Biophys. J.* **88**, 680 (2005).
- [45] www.editage.com